ACKNOWLEDGMENTS

This project was supported by award B139634411 from the U.S. Department of Labor and grant 2012-MU-FX-0002 from the Office of Juvenile Justice and Delinquency Prevention, Office of Justice Programs, U.S. Department of Justice. The study received approval from the University of Chicago's IRB (protocol 12-1112) with secondary approval from the University of Pennsylvania's IRB (protocol 818707). I gratefully acknowledge the City of Chicago and Mayor R. Emanuel, the work of the Chicago Department of Family Support Services, especially E. Diaz, J. Axelrod, A. Fernandez, and J. Welch, and the organizations that implemented the program: Phalanx Family Services, Sinai Community Institute, Saint Sabina Employment Resource Center, SGA Youth and Family Services, and Youth Guidance. I thank Chicago Public Schools partners J. Foreman, K. Klein, J. Loudon, and S. Norris; Chief R. Tracy, T. Lavery, and the Chicago Police Department; R. Goerge and Chapin Hall; R. Ander, S. Coussens, J. Davis, G. Cusick, M. Egan, H. Pollack (Chicago PI), R. Harris, N. Hess, A. Métivier, and J. Rountree for project support; and K. Charles, J. Guryan, C. Loeffler, J. Ludwig, J. MacDonald, E. Owens, S. Raudenbush, S. Sotelo, and D. Tannenbaum for helpful comments. Replication data are posted at the University of Michigan's ICPSR data depository (http://doi.org/10.3886/E18627V1); see supplementary materials section 1.5 for details. All content is the responsibility of the author and does not represent the official position or policies of the Chicago Police Department, Chicago Public Schools, Chicago Department of Family and Support Services, U.S. Department of Justice, or U.S. Department of Labor.

SUPPLEMENTARY MATERIALS

www.sciencemag.org/content/346/6214/1219/suppl/DC1
Materials and Methods
Supplementary Text
Tables S1 to S8
References (*53*–*96*)

23 June 2014; accepted 7 November 2014
10.1126/science.1257809

PALEOCLIMATE

Coherent changes of southeastern equatorial and northern African rainfall during the last deglaciation

Bette L. Otto-Bliesner,[1]* James M. Russell,[2] Peter U. Clark,[3] Zhengyu Liu,[4,5] Jonathan T. Overpeck,[6] Bronwen Konecky,[3,7] Peter deMenocal,[8] Sharon E. Nicholson,[9] Feng He,[4] Zhengyao Lu[5]

During the last deglaciation, wetter conditions developed abruptly ~14,700 years ago in southeastern equatorial and northern Africa and continued into the Holocene. Explaining the abrupt onset and hemispheric coherence of this early African Humid Period is challenging due to opposing seasonal insolation patterns. In this work, we use a transient simulation with a climate model that provides a mechanistic understanding of deglacial tropical African precipitation changes. Our results show that meltwater-induced reduction in the Atlantic meridional overturning circulation (AMOC) during the early deglaciation suppressed precipitation in both regions. Once the AMOC reestablished, wetter conditions developed north of the equator in response to high summer insolation and increasing greenhouse gas (GHG) concentrations, whereas wetter conditions south of the equator were a response primarily to the GHG increase.

The future response of African rainfall to increasing greenhouse gas (GHG) concentrations is a critical socio-economic issue, with implications for water resources, agriculture, and potential conflict (*1*), but uncertainties among model projections remain (*2*–*4*). African hydroclimate changed substantially during the last deglaciation, the most recent time period during which natural global warming was associated with increases in GHG concentrations. Numerous proxy records from Africa indicate that dry conditions during the Last Glacial Maximum (LGM) (~21,000 years ago, or 21 ka) were rapidly replaced by a much wetter interval, referred to as the African Humid Period (AHP), starting ~14.7 ka over much of Africa. Over North Africa (NA), the start of the AHP has been widely recorded in lake-level records (*5*, *6*) and proxies of aeolian and fluvial processes preserved in marine sediments from the eastern Atlantic Ocean (*7*–*10*). At the same time, a near-contemporaneous precipitation increase is also recorded in southeastern equatorial Africa (SEA) (to 9°S) by lake-level records (*11*–*14*), as well as in pollen and geochemical records from lake sediments (*14*–*16*).

Models and data establish that the initial increase of NA summer monsoonal rainfall occurred in response to increasing local insolation associated with orbital variations (*17*), amplified through feedbacks with the ocean and possibly vegetation (*18*–*20*), but the cause of the abrupt start of the AHP remains unclear. Proposed triggers include a nonlinear threshold response to gradually changing summer insolation (*8*) and/or the recovery of deep convection in the North Atlantic following cessation of a Northern Hemisphere meltwater event (*21*). Similarly, the cause for the synchronous onset of the AHP in the SEA region has remained enigmatic, as models and theory suggest that orbital forcing of local summer insolation at these latitudes should have reduced precipitation (*22*).

Here, we analyze transient simulations of the climate evolution from the LGM to the early Holocene (11 ka) with a global coupled atmosphere–ocean–sea ice–land general circulation model (CCSM3) to assess possible mechanisms for the abrupt, synchronous onset of the AHP in NA and SEA. The model has a latitude-longitude resolution of ~3.75° in the atmosphere and ~3° in the ocean and includes a dynamic global vegetation module (supplementary text). The model successfully captures the large-scale observed modern features of African climate, including seasonal shifts of winds, the intertropical convergence zone (ITCZ), and precipitation to the summer hemispheres (figs. S2 and S3). To characterize the regional precipitation responses during the deglaciation, we examine model changes in the NA region defined by 11.1° to 18.6°N and 5.6° to 20.6°E and in the SEA region defined by 0° to 7.4°S and 24.4° to 43.1°E (see supplementary text and fig. S7 for sensitivity of model results to the definitions of the regions).

The prescribed forcings and boundary conditions for the full-forcing simulation (TraCE) include orbitally forced insolation changes, increasing atmospheric concentrations of the long-lived GHGs, and retreating ice sheets and associated meltwater release to the oceans (*23*, *24*) (fig. S1). We also explore the individual contributions of orbital forcing and GHGs during the deglaciation with two sensitivity experiments: (i) TraCE orbital-only, where only the orbital forcing is allowed to vary, with all other forcings kept at their values for 17 ka, and (ii) TraCE GHG-only, where only the concentrations of the GHGs change, increasing from low concentrations at 17 ka to close to their pre-industrial concentrations by 10 ka. In both sensitivity experiments, the ice sheets and meltwater release are held constant at 17-ka conditions, and this meltwater maintains a strongly reduced Atlantic meridional overturning circulation (AMOC) afterward.

The temporal evolution of the simulated deglacial precipitation shows good agreement with individual proxy records. TraCE and a proxy record of humidity (*9*) both show dry conditions in the central Sahel at the LGM, a decrease in precipitation at ~17 ka, an abrupt increase at the onset of the Bølling-Allerød warm interval, an episode of drying during the Younger Dryas (YD) (12.9 to 11.7 ka), and an increase during the early Holocene (Fig. 1B). The total leaf-area index of simulated vegetation over the Sahel

[1]Climate and Global Dynamics Division, National Center for Atmospheric Research, Boulder, CO 80307-3000, USA. [2]Department of Earth, Environmental, and Planetary Sciences, Brown University, Providence, RI 02912, USA. [3]College of Earth, Ocean, and Atmospheric Sciences, Oregon State University, Corvallis, OR 97331, USA. [4]Center for Climatic Research and Department of Atmospheric and Oceanic Sciences, University of Wisconsin-Madison, Madison, WI 53706, USA. [5]Laboratory for Climate, Ocean and Atmosphere Studies, School of Physics, Peking University, Beijing 100871, P. R. China. [6]Department of Geosciences and Institute of the Environment, University of Arizona, Tucson, AZ 85721, USA. [7]Cooperative Institute for Research in Environmental Sciences, University of Colorado Boulder, Boulder, CO 80309, USA. [8]Department of Earth and Environmental Sciences, Columbia University, New York, NY 10027, USA. [9]Department of Earth, Ocean, and Atmospheric Science, Florida State University, Tallahassee, FL 32306, USA.
*Corresponding author. E-mail: ottobli@ucar.edu

closely parallels changes in precipitation, starting from low values signifying primarily bare ground followed by increasing values starting at ~16 ka (Fig. 1C). To the extent that precipitation and vegetation cover influence availability of sediment for aeolian transport, the temporal evolution of these simulated properties can be used to explain a record of terrigenous dust flux sourced from subtropical NA (*8*) (Fig. 1C).

Simulated deglacial changes in SEA hydrology are similar to those simulated for NA, including a near-synchronous start and subsequent persistence of the AHP. After peak dry conditions at ~17 ka, TraCE simulates a gradual increase in precipitation starting at ~16.5 ka and a large, abrupt increase at ~14.7 ka associated with the start of the AHP (Fig. 1D). These changes are observed in two SEA proxy records from Lakes Tanganyika (*16*) and Challa (*14*) (Fig. 1D), which show an abrupt onset of the AHP synchronous within a few hundred years of the precipitation increase simulated by the model. Rainfall changes in the Congo basin of western equatorial Africa, which integrate precipitation changes north and south of the equator, indicate drying from LGM to 17 ka and then increasing precipitation in both TraCE and proxy data (*25*) (Fig. 1E).

We use empirical orthogonal functions (EOFs) and their associated principal components (PCs) to extract the dominant modes of precipitation variability from the TraCE simulation and moisture balance from proxy data (table S1). The first EOF mode (EOF1) (48.0% of total variance) of the proxy data shows an in-phase relation over most of Africa that extends southward to the latitude of Lake Malawi (9° to 14°S, 34° to 35°E), whereas the associated PC1 indicates increasing moisture from the LGM to early Holocene (Fig. 2A). EOF1 of model precipitation (39.2% of total variance) and its associated PC1 (Fig. 2B) reproduce the overall spatial and temporal behavior seen in the data, except in southeastern Africa. A record of the Zambezi River discharge from this part of Africa (*26*) that is not included in the EOF analysis because of its shorter length (<17 ka) shows an out-of-phase relation with the north, consistent with the TraCE simulation.

Because seasonal insolation trends are antiphased between the two hemispheres, the in-phase relation over most of Africa shown by the data and model suggests that some other forcing must be driving precipitation change during the deglaciation. A primary role for GHG forcing of this spatially coherent hydroclimatic change is evident from the similarity of the EOF1 fields for the TraCE GHG-only (fig. S4B) and TraCE experiments (Fig. 2B). Although EOF1 for the TraCE orbital-only experiment indicates that local insolation played an important role in explaining increasingly humid conditions over NA, it has negligible loadings over the SEA region (fig. S4A), in contradiction with both proxy data and the TraCE simulation (Fig. 2).

The second EOF modes of the data and TraCE (16.4 and 17.2% of total variance, respectively) both indicate an in-phase relation of much of NA and SEA (Fig. 2, C and D). The character of the data PC2 is similar to that simulated by the model, particularly when the model PC2 is sampled at the same resolution as the data to account for potential aliasing artifacts (Fig. 2, C and D), although the model has a more muted recovery from the YD. There is a clear relation between the model PC2 (Fig. 2D) and the simulated AMOC (Fig. 1A), supporting arguments for a strong millennial modulation of African precipitation by changes in the AMOC (*21*, *27*, *28*).

We next assess the model responses to deglacial forcings that caused the AHP. In NA, our TraCE model results suggest that the AHP is largely associated with increased precipitation during the boreal summer (fig. S5A). From 17 to 11 ka, the summer monsoon over NA intensifies and shifts northward due to the combined effects of orbital and GHG forcing, though, as for all comparable climate models (*18*), not as far northward as the data suggest, highlighting a shortcoming of the models in simulating the AHP climate of this northerly region. Sea-level pressure decreases over NA, and attendant increased southwesterly flow brings moisture from the Atlantic into NA and enhances precipitation in a broad east-west band over the Sahel and southern Sahara to ~22°N (Fig. 3A). For the other seasons, simulated precipitation remains

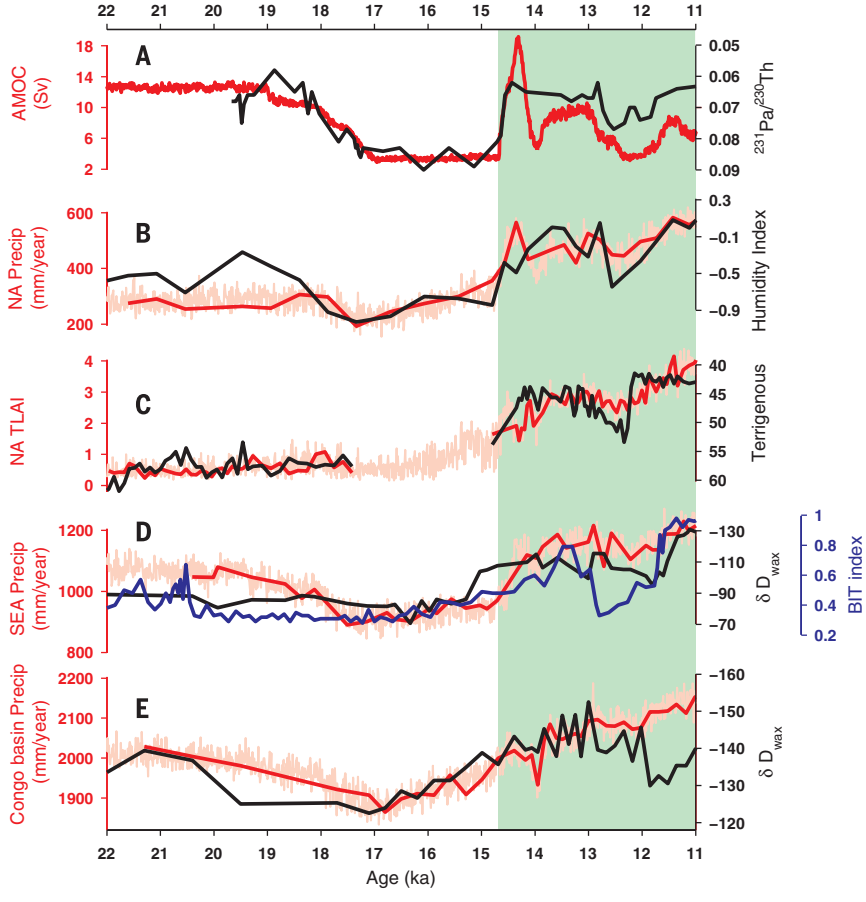

Fig. 1. TraCE simulation with all deglacial forcings (fig. S1) in comparison to proxy data. Model variables are plotted as decadal means (light red) and as sampled at temporal resolution of data (darker red). See Fig. 3 for definition of model NA and SEA regions. (**A**) ^{231}Pa/^{230}Th ratio at Bermuda rise (GGC5 core, 33°42′N, 57°35′W) as a proxy for AMOC export (black) (*32*) and model maximum AMOC (Sv). (**B**) GeoB7920-2 (20°45′N, 18°35′W) continental humidity index (black) (*9*) and model NA precipitation (millimeters per year). (**C**) Ocean Drilling Program site 658C (20°45′N, 18°35′W) terrigenous percentage (black) (*8*) and model NA total leaf area index (TLAI) (square meters per square meters). (**D**) Lake Tanganyika (6°42′S, 29°50′E) hydrogen isotopic composition of leaf waxes (δD_{wax}) (per mil versus Vienna standard mean ocean water, black) (*16*), Lake Challa (3°19′S, 37°42′E) branched and isoprenoid tetraether (BIT) index (blue) (*14*), and model SEA precipitation (millimeters per year). (**E**) GeoB6518 (5°35′S, 11°13′E) δD_{wax} (black) (*25*) and Congo Basin (7.4°N to 11.1°S, 13.1°E to 28.1°E) model precipitation (millimeters per year). Green shading delineates AHP.

low throughout the entire simulation from the LGM to the early Holocene (fig. S5A).

Results from our single forcing experiments indicate that GHG and orbital forcings each contributed to the enhanced summer monsoon and precipitation increase across NA from 17 to 11 ka seen in the TraCE results. TraCE GHG-only shows an increase in precipitation in the southern Sahel but little broadening of the tropical rainbelt (Fig. 3B). TraCE orbital-only similarly shows enhanced precipitation in the Sahel while additionally expanding the monsoon precipitation northward (Fig. 3C). In the central Sahel, orbital forcing explains ~60% of the precipitation increase from 17 to 11 ka and GHG forcing explains the remaining ~40% (fig. S6).

The simulated AHP in SEA is associated with increased precipitation from the austral spring through fall, whereas simulated precipitation remains low during the austral winter [June-July-August (JJA)] throughout the deglacial period (fig. S5B). TraCE suggests a different seasonal nature of SEA precipitation at LGM than during the AHP, with austral summer [December-January-February (DJF)] precipitation explaining proportionately more of the annual precipitation (fig. S5B). In general, DJF precipitation increases from 17 to 11 ka throughout the southern tropics, extending from the Atlantic Ocean, across Africa, and into the Indian Ocean (Fig. 3D). The single forcing experiments indicate that most of this response (90%) is from the increase in GHGs (fig. S6), which caused DJF precipitation over the SEA region to increase from 17 to 11 ka (Fig. 3E). In the TraCE orbital-only experiment, on the other hand, decreased DJF insolation cools the land relative to the ocean, slightly weakening convection and precipitation over SEA near Lake Tanganyika while enhancing convection and precipitation over the Indian Ocean from 17 to 11 ka (Fig. 3F).

Proxy records and TraCE also exhibit consistent patterns and amplitude of changes in sea surface temperature (SST) around Africa from 17 to 11 ka (Fig. 4A and table S2). The differential warming in the northern Atlantic Ocean relative to the south, and in the western Indian Ocean relative to the east, is important in driving the increased precipitation in NA and SEA, respectively. The single forcing experiments indicate that increases in GHGs are primarily responsible for the overall SST increases and their regional patterns (Fig. 4B). Orbital forcing further reduces the meridional SST gradient in the North Atlantic, with warming north of the equator and slight cooling at and south of the equator (Fig. 4C).

Although our single forcing experiments demonstrate that GHG forcing played an important role in the moistening trends over NA (and particularly SEA), linking precipitation changes between the hemispheres, our TraCE simulation shows that millennial-scale changes in the AMOC are critical in synchronizing the onset of the AHP in these regions (Figs. 1 and 2). Our simulation agrees with other modeling studies (*27*–*29*) in finding that freshwater added to North Atlantic sites of deepwater formation reduces the AMOC, with an attendant shift in the ITCZ southward over the Atlantic Ocean in response to higher SSTs south of the equator and cooling north of the equator and a reduction of precipitation over NA. The bipolar Atlantic SST response and southward shift in the ITCZ also explain the opposite loadings of model EOF2 between North Africa and western equatorial Africa (Fig. 2D).

Cooling over the North Atlantic is also rapidly transmitted eastward into Europe and Asia through the atmosphere (*30*), enhancing the boreal winter Mediterranean-Arabian anticyclone. This results in northerly wind anomalies advecting cool and dry air over East Africa and the western Indian Ocean. This in turn results in cooler western Indian Ocean SSTs both north and south of the equator and a reduction of SEA precipitation (supplementary text and fig. S8). At ~14.7 ka, the cessation of meltwater forcing, the rapid resumption of AMOC, and the associated SST changes triggered abrupt and synchronous increases in precipitation in NA and SEA associated with the start of the AHP.

The spatial pattern of precipitation in EOF1 (Fig. 2B) is markedly similar to the historical patterns (*31*), as well as CMIP5 ensemble projection for precipitation changes over tropical Africa by the end

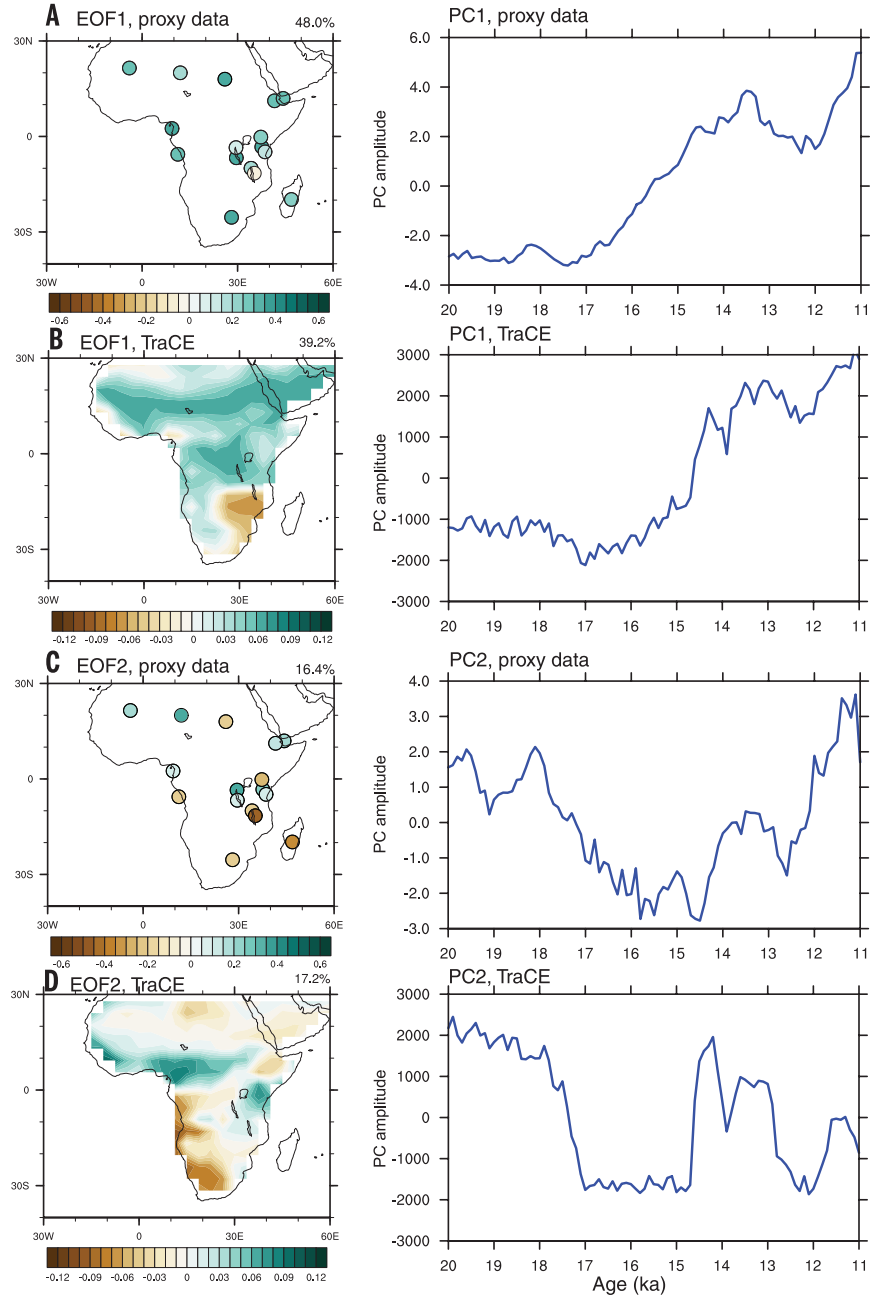

Fig. 2. EOFs and associated PCs for the deglacial period 20 to 11 ka. EOF1 and PC1 of (**A**) proxy data for moisture availability and (**B**) TraCE annual precipitation (millimeters per year). (**C** and **D**) Same as (A) and (B) except for EOF2 and PC2. Model results and proxy records (table S1) are interpolated to the same 100-year resolution.

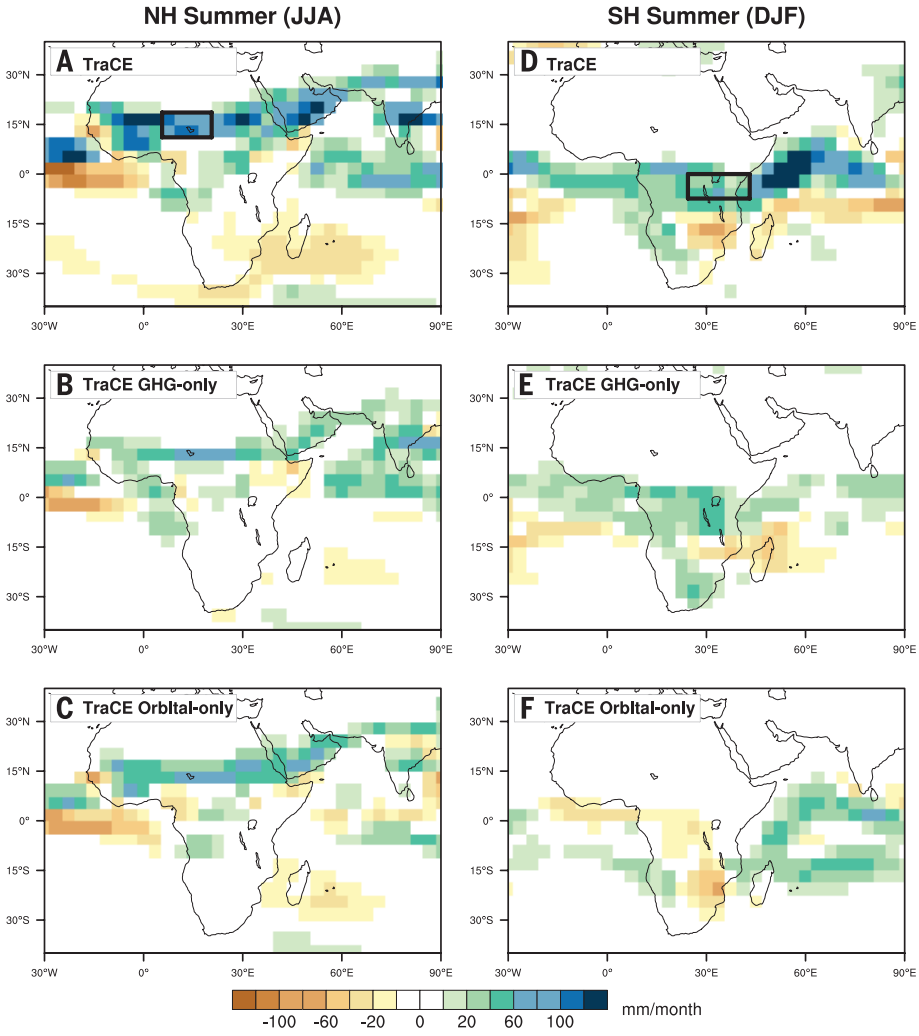

Fig. 3. Deglacial precipitation change (millimeters per month), 11 ka minus 17 ka, as simulated by the model. (**A** and **D**) TraCE, (**B** and **E**) TraCE GHG-only, and (**C** and **F**) TraCE orbital-only. The box in (A) represents the NA region used to characterize model results (11.1° to 18.6°N, 5.6° to 20.6°E); the box in (D) represents the SEA region (0° to 7.4°S, 24.4° to 43.1°E). NH, Northern Hemisphere; SH, Southern Hemisphere. JJA, June-July-August; DJF, December-January-February.

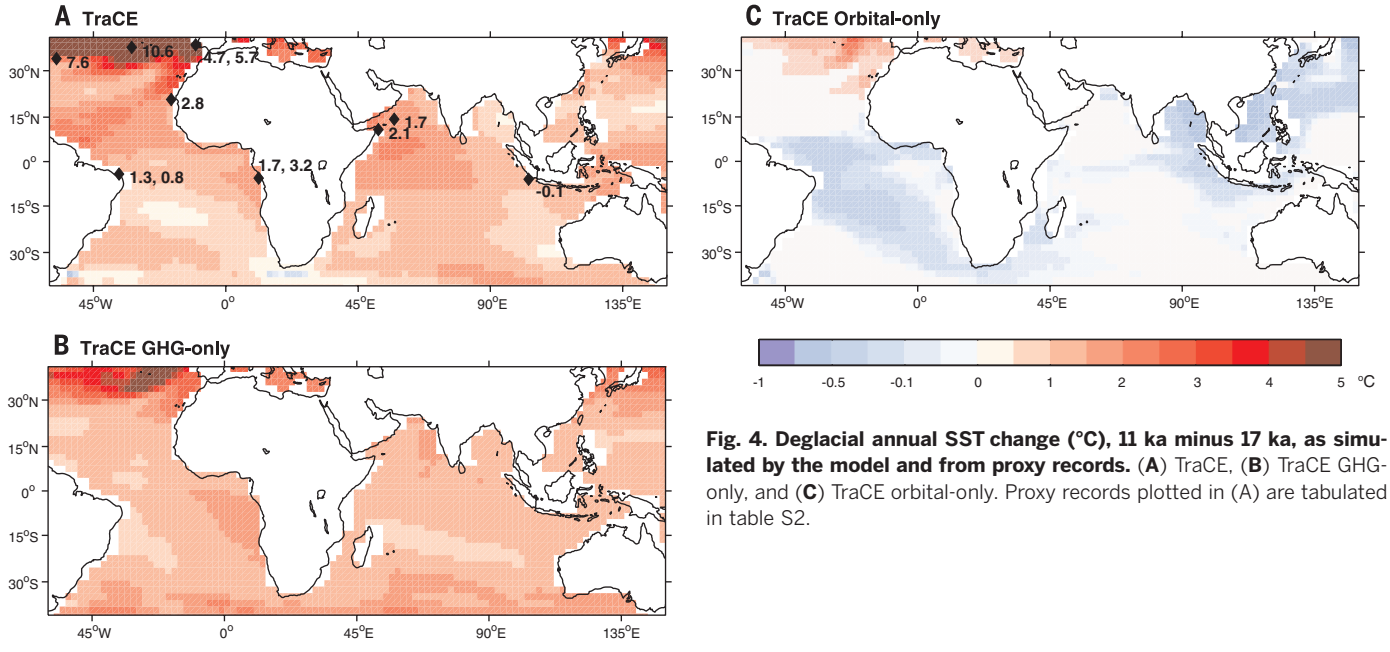

Fig. 4. Deglacial annual SST change (°C), 11 ka minus 17 ka, as simulated by the model and from proxy records. (**A**) TraCE, (**B**) TraCE GHG-only, and (**C**) TraCE orbital-only. Proxy records plotted in (A) are tabulated in table S2.

of this century (*3*). Although multiple forcings influenced African climate during the deglaciation, the agreement between proxy records and our simulated evolution of rainfall indicates that the processes and sensitivity of GHG-driven rainfall change are well simulated in our fully coupled global climate model. This lends confidence to the CMIP5 climate model ensemble projections of future precipitation change over tropical Africa at the continental scale.

REFERENCES AND NOTES

1. I. Niang *et al.*, "Africa," in *Climate Change 2014: Impacts, Adaptation, and Vulnerability. Part B: Regional Aspects. Contribution of Working Group II to the Fifth Assessment Report of the Intergovernmental Panel on Climate Change*, V. R. Barros *et al.*, Eds. (Cambridge Univ. Press, New York, 2014), pp. 1199–1265.
2. A. Giannini, M. Biasutti, I. M. Held, A. H. Sobel, *Clim. Change* **90**, 359–383 (2008).
3. M. Collins *et al.*, "Long-term climate change: Projections, commitments and irreversibility," in *Climate Change 2013: The Physical Science Basis. Contribution of Working Group I to the Fifth Assessment Report of the Intergovernmental Panel on Climate Change*, T. F. Stocker *et al.* Eds. (Cambridge Univ. Press, New York, 2013), pp. 1029–1136.
4. J. H. Christensen *et al.*, "Climate phenomena and their relevance for future regional climate change," in *Climate Change 2013: The Physical Science Basis. Contribution of Working Group I to the Fifth Assessment Report of the Intergovernmental Panel on Climate Change*, T. F. Stocker *et al.*, Eds. (Cambridge Univ. Press, New York, 2013), pp. 1217–1308.
5. T. M. Shanahan *et al.*, *Palaeogeogr. Palaeoclimatol. Palaeoecol.* **242**, 287–302 (2006).
6. F. A. Street, A. T. Grove, *Quat. Res.* **12**, 83–118 (1979).
7. J. M. Cole, S. L. Goldstein, P. N. deMenocal, S. R. Hemming, F. E. Grousset, *Earth Planet. Sci. Lett.* **278**, 257–266 (2009).
8. P. deMenocal *et al.*, *Quat. Sci. Rev.* **19**, 347–361 (2000).
9. R. Tjallingii *et al.*, *Nat. Geosci.* **1**, 670–675 (2008).
10. S. Weldeab, D. W. Lea, R. R. Schneider, N. Andersen, *Science* **316**, 1303–1307 (2007).
11. F. Gasse, F. Chalie, A. Vincens, M. A. J. Williams, D. Williamson, *Quat. Sci. Rev.* **27**, 2316–2340 (2008).
12. T. C. Johnson *et al.*, *Science* **273**, 1091–1093 (1996).
13. M. M. McGlue *et al.*, *J. Paleolimnol.* **40**, 635–653 (2008).
14. D. Verschuren *et al.*, *Nature* **462**, 637–641 (2009).
15. R. Bonnefille, F. Chalie, *Global Planet. Change* **26**, 25–50 (2000).
16. J. E. Tierney *et al.*, *Science* **322**, 252–255 (2008).
17. J. E. Kutzbach, B. L. Otto-Bliesner, *J. Atmos. Sci.* **39**, 1177–1188 (1982).
18. P. Braconnot *et al.*, *Nat. Clim. Change* **2**, 417–424 (2012).
19. J. E. Kutzbach, Z. Liu, *Science* **278**, 440–443 (1997).
20. O. Timm, P. Kohler, A. Timmermann, L. Menviel, *J. Clim.* **23**, 2612–2633 (2010).
21. F. A. Street-Perrott, R. A. Perrott, *Nature* **343**, 607–612 (1990).
22. Z. Liu, B. Otto-Bliesner, J. Kutzbach, L. Li, C. Shields, *J. Clim.* **16**, 2472–2490 (2003).
23. Z. Liu *et al.*, *Science* **325**, 310–314 (2009).
24. Z. Liu *et al.*, *Proc. Natl. Acad. Sci. U.S.A.* **109**, 11101–11104 (2012).
25. J. W. H. Weijers, E. Schefuß, S. Schouten, J. S. Sinninghe Damsté, *Science* **315**, 1701–1704 (2007).
26. E. Schefuß, H. Kuhlmann, G. Mollenhauer, M. Prange, J. Pätzold, *Nature* **480**, 509–512 (2011).
27. M. Kageyama *et al.*, *Clim. Past* **9**, 935–953 (2013).
28. R. J. Stouffer *et al.*, *J. Clim.* **19**, 1365–1387 (2006).
29. S. Mulitza *et al.*, *Paleoceanography* **23**, PA4206 (2008).
30. B.-W. Dong, R. T. Sutton, *Geophys. Res. Lett.* **29**, 18-1–18-4 (2002).
31. S. E. Nicholson, *Holocene* 10.1177/0959683614551230 (2014).
32. J. F. McManus, R. Francois, J.-M. Gherardi, L. D. Keigwin, S. Brown-Leger, *Nature* **428**, 834–837 (2004).

ACKNOWLEDGMENTS

We thank the reviewers for comments that improved the manuscript. The National Center for Atmospheric Research (NCAR) is sponsored by the NSF. This research was also supported by the Office of Science (Biological and Environmental Research), U.S. Department of Energy (DOE), the NSF Paleo Perspectives on Climate Change (P2C2) program, and NSF grant AGS 1160750. This research used resources of the Oak Ridge Leadership Computing Facility, located in the National Center for Computational Sciences at Oak Ridge National Laboratory, which is supported by the DOE Office of Science. The observed data are downloadable from the National Oceanic and Atmospheric Administration Paleoclimatology (www.ncdc.noaa.gov/data-access/paleoclimatology-data) and/or Pangaea (www.pangaea.de/). The model data are downloadable from the Earth System Gateway at NCAR (www.earthsystemgrid.org/home.htm).

SUPPLEMENTARY MATERIALS

www.sciencemag.org/content/346/6214/1223/suppl/DC1
Supplementary Text
Fig. S1 to S8
Tables S1 and S2
References (*33*–*72*)

4 August 2014; accepted 6 November 2014
10.1126/science.1259531

OCEANOGRAPHY

Multidecadal warming of Antarctic waters

Sunke Schmidtko,[1,2]* Karen J. Heywood,[1] Andrew F. Thompson,[3] Shigeru Aoki[4]

Decadal trends in the properties of seawater adjacent to Antarctica are poorly known, and the mechanisms responsible for such changes are uncertain. Antarctic ice sheet mass loss is largely driven by ice shelf basal melt, which is influenced by ocean-ice interactions and has been correlated with Antarctic Continental Shelf Bottom Water (ASBW) temperature. We document the spatial distribution of long-term large-scale trends in temperature, salinity, and core depth over the Antarctic continental shelf and slope. Warming at the seabed in the Bellingshausen and Amundsen seas is linked to increased heat content and to a shoaling of the mid-depth temperature maximum over the continental slope, allowing warmer, saltier water greater access to the shelf in recent years. Regions of ASBW warming are those exhibiting increased ice shelf melt.

The Antarctic ice sheet is the largest reservoir of terrestrial ice and is a significant contributor to sea level rise in a warming climate (*1*). Massive ice shelf disintegration and rapid acceleration of glacial flow have occurred in recent decades (*2*) or are potentially looming (*3*). These events are generally linked to enhanced basal melt (*4*, *5*), which reduces buttressing and accelerates glacier flow. An increase in basal melt may be linked to stronger sub–ice shelf circulation of Circumpolar Deep Water (CDW). It is not known whether changes in the delivery of warm water to the underside of the ice shelf are caused by increased heat content, increased volume flux responding to changes in wind and buoyancy forcing, or some combination of the two (*6*, *7*). Here, we focus on documenting long-term temperature and salinity changes in ocean properties over the continental shelf and slopes.

We refer to the water occupying the sea floor on the Antarctic continental shelf as Antarctic Continental Shelf Bottom Water (ASBW) and the temperature minimum layer, representing the remnant of the winter mixed layer, as Winter Water (WW). Atmospheric processes, adjacent water masses, ice shelf and continental freshwater fluxes, and bathymetry-dependent cross-shelf water exchange at the shelf break determine the hydrographic properties of ASBW. Hence, ASBW is a mixture of CDW, WW, and waters originating from continental runoff, ice shelf melting, or sea ice formation. Temporal changes in ASBW may represent changes either in formation processes or in properties of source waters. ASBW has freshened in the Ross Sea (*8*) and northwest Weddell Sea (*9*), with the former generally linked to enhanced upstream ice shelf melt. Recent research has identified large-scale warming of both CDW north of 60°S (*10*) and Antarctic Bottom Water (AABW) (*11*). However, statistically significant long-term warming of ASBW has been observed only in localized regions (*12*), and trends in CDW properties over the Antarctic continental slope have not previously been described in detail.

Using a comprehensive compilation of observational data sets (table S1) [(*13*) and supplementary materials], we found that temporal trends in ASBW temperature and salinity have a distinct regional pattern (Fig. 1). The Bellingshausen Sea and Amundsen Sea shelves show significant warming (0.1° to 0.3°C decade^{-1}; Fig. 1, C and E) and salinification (0.01 to 0.04 g kg^{-1} decade^{-1}; Fig. 1, D and F) since the 1990s, when sufficient observations became available (fig. S2). The Ross Sea is freshening (−0.027 ± 0.012 g kg^{-1} decade^{-1}), and the western Weddell Sea reveals a slight cooling (−0.05° ± 0.04°C decade^{-1}) and freshening (−0.01 ± 0.007 g kg^{-1} decade^{-1}); older measurements allow these trends to be calculated from the 1970s. The Cosmonaut Sea is

[1]Centre for Ocean and Atmospheric Sciences, School of Environmental Sciences, University of East Anglia, Norwich NR4 7TJ, UK. [2]GEOMAR Helmholtz Centre for Ocean Research Kiel, Düsternbrooker Weg 24, 24105 Kiel, Germany. [3]Environmental Science and Engineering, California Institute of Technology, Pasadena, CA 91125, USA. [4]Institute of Low Temperature Science, Hokkaido University, Sapporo 060-0819, Japan.
*Corresponding author. E-mail: sschmidtko@geomar.de

Coherent changes of southeastern equatorial and northern African rainfall during the last deglaciation

Bette L. Otto-Bliesner *et al.*

Science **346**, 1223 (2014);
DOI: 10.1126/science.1259531